








Coherent control of the orbital occupation driving the insulator-to-metal Mott transition in V_2O_3

Paolo Franceschini,^{1,2,3,*} Veronica R. Policht⁴,, Alessandra Milloch^{1,2,3},, Andrea Ronchi^{1,2,3,†}, Selene Mor,^{1,2} Simon Mellaerts³,, Wei-Fan Hsu³,, Stefania Pagliara,^{1,2} Gabriele Ferrini,^{1,2} Francesco Banfi,⁵ Michele Fabrizio⁶,,
Mariela Menghini,⁷ Jean-Pierre Locquet³,, Stefano Dal Conte,⁴ Giulio Cerullo,⁴ and Claudio Giannetti^{1,2,8,‡}

¹*Department of Mathematics and Physics, Università Cattolica del Sacro Cuore, IT-25133 Brescia, Italy*

²*ILAMP (Interdisciplinary Laboratories for Advanced Materials Physics), Università Cattolica del Sacro Cuore, IT-25133 Brescia, Italy*

³*Department of Physics and Astronomy, KU Leuven, B-3001 Leuven, Belgium*

⁴*Department of Physics, Politecnico di Milano, IT-20133 Milano, Italy*

⁵*FemtoNanoOptics group, Université de Lyon, CNRS, Université Claude Bernard Lyon 1, Institut Lumière Matière, F-69622 Villeurbanne, France*

⁶*Scuola Internazionale Superiore di Studi Avanzati (SISSA), IT-34136 Trieste, Italy*

⁷*IMDEA-Nanociencia, E-28049 Madrid, Spain*

⁸*CNR-INO (National Institute of Optics), via Branze 45, IT-25123 Brescia, Italy*



(Received 4 July 2022; revised 24 January 2023; accepted 10 April 2023; published 26 April 2023)

Managing light-matter interactions on timescales faster than the loss of electronic coherence is key for achieving full quantum control of the final products in solid-solid transformations. In this Letter, we demonstrate coherent optical control of the orbital occupation that determines the insulator-to-metal transition in the prototypical Mott insulator V_2O_3 . Selective excitation of a specific interband transition with two phase-locked light pulses manipulates the occupation of the correlated bands in a way that depends on the coherent evolution of the photoinduced superposition of states. A comparison between experimental results and numerical solutions of the optical Bloch equations provides an electronic coherence time on the order of 5 fs. Temperature-dependent experiments suggest that the electronic coherence time is enhanced in the vicinity of the insulator-to-metal transition critical temperature, thus highlighting the role of fluctuations in determining the electronic coherence. These results open different routes to selectively switch the functionalities of quantum materials and coherently control solid-solid electronic transformations.

DOI: [10.1103/PhysRevB.107.L161110](https://doi.org/10.1103/PhysRevB.107.L161110)

The ability to control matter transformations along quantum coherent pathways is key for opening new frontiers in condensed matter physics, with a broader impact on the development of novel quantum technologies [1,2]. In contrast with conventional state transitions, in which electrons can be considered as incoherent degrees of freedom instantaneously coupled to external reservoirs (phonons, vibrations, and charge or spin excitations), coherent control protocols are based on the creation of a quantum coherent superposition of states that freely evolve and determine the output of the transformation before any decoherence process takes place [3,4].

Early efforts to achieve optical coherent control exploited the long coherence times ($T_2 \gtrsim 1$ ps) of atomic and molecular systems to control the output of specific chemical reactions [4–9]. The solid state counterpart, i.e., the control of the output of a thermodynamic phase transition, is far more challenging given decoherence timescales on the order of a few fem-

toseconds due to the extremely efficient coupling of charge excitations to the environment. Recent attempts at coherent control in solid state systems have demonstrated optical control of the insulator-to-metal transition in organic correlated crystals [10] and indium wires [11] by exploiting the relatively long-lived vibrational coherence. In these studies, a combination of two short phase-coherent light pulses was shown to enable the switching of the structural phase of the system in a way that depends on the instantaneous nuclear position during the oscillation of the structural amplitude modes connecting the two phases [11]. Coherent schemes have additionally been implemented to control the dynamics of photoemitted electrons in metals and superconductors [12–15] and the instantaneous electronic photocurrents in semiconductors [16,17], without driving any phase transformation in the material. To date, managing the coherent dynamics of electronic states that control the output of a solid-solid phase transition is still an unexplored field.

Here, we report evidence of the electronic coherence of the interband transitions relevant for the insulator-to-metal transition (IMT) of V_2O_3 by means of optical manipulation with two extremely short phase-locked light pulses. V_2O_3 undergoes a phase transition at $T_{\text{IMT}} \sim 180$ K from a low-temperature antiferromagnetic monoclinic insulator (AFI) to a high-temperature paramagnetic corundum metal (PM). The

*Present address: CNR-INO (National Institute of Optics), via Branze 45, IT-25123 Brescia, Italy; paolo.franceschini@ino.cnr.it

†Present address: Pirelli Tyre S.p.A, viale Piero e Alberto Pirelli 25, IT-20126 Milano, Italy.

‡claudio.giannetti@unicatt.it

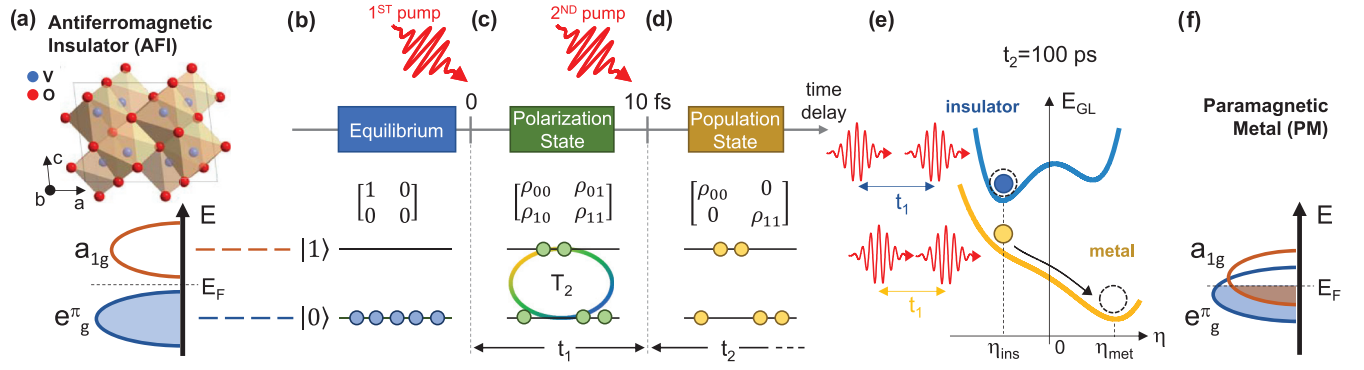


FIG. 1. Cartoon of the experiment. (a) Crystal structure and sketch of the electronic band structure near the Fermi level (E_F) for the antiferromagnetic insulating (AFI) phase of V_2O_3 . (b)–(d) Two-level system representing the orbital population excited by two coherent pump pulses and (e) free-energy (E_{GL}) diagram showing the phase of the system. The ground and excited many-body states, characterized by different occupations of the e_g^π and a_{1g} electronic levels, are identified as $|0\rangle$ and $|1\rangle$. (b) When the first pump pulse arrives, the system is at equilibrium (insulating phase), i.e., in the ground state $|0\rangle$. (c) After the first excitation, the system is left in a *polarization state*, described by nonzero off-diagonal terms (ρ_{01} and ρ_{10}) of the density matrix. The second phase-coherent pulse manipulates the coherent superposition of levels $|0\rangle$ and $|1\rangle$ within the coherence time T_2 . After the coherent photoexcitation, the system is left in a *population state* (d), with zero off-diagonal terms, which evolves towards a thermal state. (e) The t_1 -dependent population determines the energy potential profile and, consequently, the final state of the system at large delay time, $t_2 = 100$ ps. (f) Electronic band structure near the Fermi level (E_F) for the paramagnetic metallic (PM) phase of V_2O_3 . Crystal structure in (a) adapted from Ref. [18], and electronic band structure in (a) and (f) adapted from Ref. [19].

combination of strong on-site Coulomb repulsion, crystal field splitting, and trigonal distortion of the V-O octahedra gives rise to a manifold of electronic states within the vanadium 3d levels. In particular, the conductive state of V_2O_3 is mainly determined by the occupation of the lowest levels, i.e., the e_g^π doublet, mainly oriented in the a - b plane, and the upper a_{1g} singlet, mainly oriented along the c axis [see Fig. 1(a)]. At T_{IMT} , the shortening of the V-V dimers along the hexagonal c axis favors an increase of the a_{1g} occupation ($n_{a_{1g}}$) at the expense of the e_g^π one ($n_{e_g^\pi}$) and drives the transition from a Mott insulator to a metal [20–22]. The a_{1g} orbital occupation, though being finite in both phases [21,23,24], jumps upwards at the transition and thus can be considered as its control parameter.

Optical transitions in the visible region can be used to nonthermally manipulate $n_{a_{1g}}$. Visible light pulses have been demonstrated to trigger the transformation from an insulator to a metastable metal by the suitable excitation of interband transitions [22,25–28]. The underlying concept of the coherent control protocol is based on the excitation of the $e_g^\pi \rightarrow a_{1g}$ optical transition by two phase-coherent pulses [Figs. 1(b)–1(e)]. For simplicity, we will refer to the insulating many-body ground state as $|0\rangle$ and to the excited state as $|1\rangle$. The first pump pulse excites the insulating ground state, characterized by the equilibrium occupation $n_{a_{1g}}$, and creates a quantum superposition of states $|\Psi\rangle = p_0|0\rangle + p_1|1\rangle$, where $|p_{0(1)}|^2$ is the time-dependent probability of finding the system in the state $|0(1)\rangle$ [Fig. 1(c)]. If we consider the density matrix $\hat{\rho} = |\Psi\rangle\langle\Psi|$, the quantum polarization state generated by the first pump pulse is described by nonzero off-diagonal terms ρ_{nm} , which are eventually destroyed by the decoherence brought by the environment, here composed by phonons, and spin and charge excitations. The following interaction with the second phase-locked pump pulse leaves the system in a population state characterized by increased $n_{a_{1g}}$, encoded in the diagonal population term (ρ_{11}) of the density matrix [Fig. 1(d)]. The

orbital population variation induced by the excitation protocol thus depends on the instantaneous polarization state at the time of the interaction with the second pump pulse. As demonstrated in Ref. [22], the IMT can be described via a Landau-Ginzburg energy functional E_{GL} [Fig. 1(e)], which takes the form

$$E_{GL}(n_{a_{1g}}) \propto [\eta - \eta_{met}]^2 [\eta - \eta_{ins}]^2 - g(n_{a_{1g}}, T)\eta, \quad (1)$$

where η is the order parameter assuming the values $\eta_{met} > 0$ and $\eta_{ins} < 0$ in the metallic and insulating phases, respectively. The effect of the interaction with the light pulses is accounted for by the coupling term $g(n_{a_{1g}}, T)$, which is negative at equilibrium for $T < T_{IMT}$ and becomes positive, thus stabilizing the metallic phase, when either $n_{a_{1g}}$ is increased by the pump pulses or $T > T_{IMT}$. As a consequence, by preparing the $|\Psi\rangle$ many-body state we can coherently control the final population difference $n_{a_{1g}} - n_{e_g^\pi} = \rho_{11} - \rho_{00}$ and, in turn, the free energy of the system. The combined action of the two phase-coherent pump pulses thus leaves the system in a nonequilibrium configuration, which evolves towards a metastable metallic state, characterized by η_{met} , within the timescale (~ 50 ps) necessary to complete the electronic and structural transformation [22,28].

In conventional incoherent excitation schemes, the amount of material undergoing the phase transition is strictly proportional to the intensity of the excitation light. In contrast, the coherent dynamics addressed by the two-pump coherent experiment proposed here results in multiple effects. First, if the two-level system is excited by two phase-coherent pulses with photon energy $\hbar\omega_p = \hbar\omega_{01} + \delta\omega$, where $\hbar\omega_{01}$ is the energy difference between the two levels and $\delta\omega$ the energy detuning, the oscillation of $\rho_{11} - \rho_{00}$ as a function of the delay between the two coherent pumps is pinned to ω_{01} , in the limit of large T_2 . This leads to a detectable frequency difference between the time-domain linear interferogram of the two pump pulses and the signal related to the photoinduced IMT. Second, if the

dephasing time of the electronic coherence state generated by the first pulse is comparable to or longer than the pulse width, coherence effects can be observed beyond the strict temporal overlap of the two pump pulses. In particular, oscillations of the final population can survive longer than the time-domain linear interferogram of the two pump pulses, thus leading to a variation $\delta\gamma = \gamma_s - \gamma_p$ of the spectral width of the signal (γ_s) relative to the spectral width of the pump pulse (γ_p), which is related to the IMT.

In order to resolve possible signatures of the coherent dynamics described above, it is crucial to maintain a high degree of phase coherence between the two pump pulses and to accurately tune the experimental parameters so as to maximize the effects. This experiment requires temporally short and spectrally broadband light pulses whose spectral widths cover the spectral region of the expected frequency shift, while providing enough excess energy to overcome the insulator-to-metal transformation barrier [see Sec. S2 in the Supplemental Material (SM) [29]]. The choice of the experimental parameters was informed by the numerical solution to the optical Bloch equations (OBEs) (see Sec. S3 in the SM [29]), which allows us to simulate the dynamics of the ρ_{11} population in the presence of an effective decoherence driven by the coupling of the electronic wave functions with the environment. Considering realistic pulse durations (~ 30 fs) and reasonable tunability (~ 50 meV, see Fig. S3 in the SM [29]) around ω_{01} , signatures of coherent effects are observable for T_2 as small as a few femtoseconds, provided a phase stability of the order of $1/1000$ of the optical cycle is achieved.

In the present work, the IMT is optically triggered by means of two phase-coherent pump pulses (with duration < 28 fs as measured by polarization-gated frequency-resolved optical gating) generated by translating-wedge-based identical-pulse-encoding system (TWINS) technology, a collinear interferometer based on birefringent wedges capable of tuning the relative delay (t_1) between the two pulse replicas with attosecond precision and excellent phase stability (~ 2 as, see Sec. S4 in the SM for more details) [30–33]. A third optical pulse arriving at fixed delay t_2 after the excitation pulses probes the final state of the system, thus providing a t_1 -dependent pump-induced relative reflectivity variation, $\delta R/R(t_1, t_2)$ (see Sec. S5 in the SM for a detailed description of the experimental setup [29]). In this Letter, we focus on the interband electronic transition at ~ 2.4 eV (Fig. S1 in the SM [29]), which is a transition between the e_g^* and a_{1g} bands and is particularly sensitive to the insulator-to-metal transformation [28]. The sample under study consists of a 50-nm-thick V_2O_3 thin film deposited by oxygen assisted molecular beam epitaxy (MBE) on a (0001)-oriented sapphire (Al_2O_3) substrate, with the c axis perpendicular to the surface [34].

We first observe the dynamics of the incoherent IMT by performing a conventional pump-probe experiment, corresponding to the case of $t_1 = 0$, at $T = 140$ K. For fluences higher than ~ 4 mJ/cm², the $\delta R/R(t_2)$ signal at long delays ($t_2 > 50$ ps) shows the same reflectivity decrease observed during the thermally driven IMT [22]. For intermediate fluences (< 0.5 mJ/cm²), as those used for the trace reported in Fig. 2(a) and in the following experiments, the signal is linearly proportional to the pump excitation and to the metallic filling fraction variation [28]. The relative reflectivity

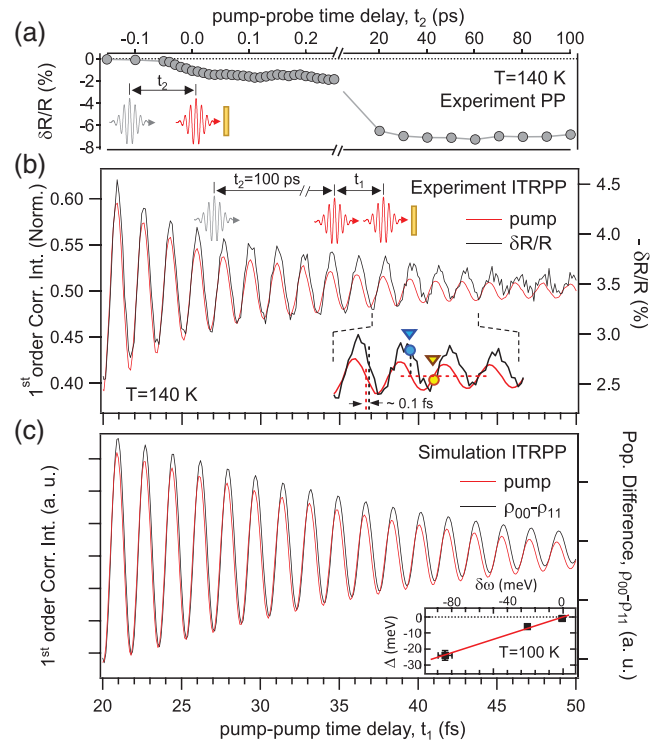


FIG. 2. Interferometric time-resolved pump-probe (ITRPP). (a) Relative reflectivity variation $\delta R/R(t_2)$ as a function of t_2 detected at 2.42 eV photon energy [standard pump-probe (PP) experiment as sketched in the inset]. (b) Relative reflectivity variation $\delta R/R(t_1)$ detected at 2.42 eV photon energy as a function of the pump-pump delay t_1 (black line), at a fixed probe delay $t_2 = 100$ ps, compared with the first-order correlation function of the pump pulse (red line). The experimental data in (a) and (b) have been obtained at $T = 140$ K with an incident pump fluence of 0.4 mJ/cm². Inset: Expanded view highlighting the different $\delta R/R$ value (markers) at t_1 delay times corresponding to the same pump intensity: $t_1 = 39.8$ fs (blue marker) and $t_1 = 40.7$ fs (yellow marker). (c) Calculated two-level population difference as a function of the pump-pump delay t_1 (black line) compared with the first-order correlation function of the pump pulse (red line). (c) Inset: Excitation-energy-dependent shift at fixed temperature $T = 100$ K. A linear model (red line) has been fitted to the experimental data (black markers). The simulation has been performed by solving OBE with $T_2 = 5$ fs and $\delta\omega = 0.06$ eV. Signals in (b) and (c) are shown for $t_1 \geq 20$ fs to highlight the frequency shift.

variation dynamic is characterized by a buildup of the order of few tens of ps corresponding to the photoinduced nucleation and growth of metallic domains [28,35]. At $t_2 = 100$ ps, the phase transformation is complete as indicated by the t_2 -dependent signal [Fig. 2(a)]. Therefore this t_2 value is chosen as the detection time for the interferometric experiment, in which the transient $\delta R/R(t_1)$ signal is recorded as a function of t_1 . The t_1 -dependent relative reflectivity variation signal is reported in Fig. 2(b). The $\delta R/R(t_1)$ signal (black solid line) is shown together with the linear interferogram (first-order correlation function) of the pump pulse pair (red solid line). The oscillatory pattern of $\delta R/R$ shows a progressive dephasing with respect to the pump interferogram, thus suggesting a frequency shift between the two signals. The phase

difference accumulated after 25 oscillations corresponds to a delay of ~ 100 as, which is well above the phase stability of our setup. The observed dephasing indicates that the correlated $\delta R/R(t_1)$ signal, proportional to the amount of material driven into the metallic phase, is no longer proportional to the pump intensity. The inset of Fig. 2(b) shows that, given the same pump intensity for example at $t_1 = 39.8$ fs and $t_1 = 40.7$ fs, $\delta R/R(t_1)$ after 100 ps assumes two values differing by about 7%. The frequency shift between the two interferograms in Fig. 2(b) is evaluated by comparing the central frequencies of the spectra obtained by Fourier transforming the time-domain data with respect to t_1 . Details of the analysis process can be found in Sec. S5 of the SM [29]. We find that the frequency of the $\delta R/R(t_1)$ signal is redshifted by an amount corresponding to $\Delta = (4 \pm 1)$ meV with respect to the pump linear interferogram. At the same time, oscillations of the $\delta R/R(t_1)$ signal persists for a longer time interval than the temporal width of the pump interferogram, as indicated by the spectral width variation $\delta\gamma/\gamma_p = -(2.6 \pm 0.3)\%$. From the numerical solution of OBE, we pinpoint that the energy shift Δ depends on the coherence time and that it is smaller than the detuning, $|\Delta| < |\delta\omega|$, for finite T_2 . In the limit $T_2 \rightarrow \infty$, Δ coincides with $\delta\omega$ (see Sec. S2 in the SM for more details [29]).

The experimental data shown in Fig. 2 are compared to the results of the OBE simulations, which are used to compute the time-dependent population difference, $\rho_{00} - \rho_{11}(t_1)$, following the interaction with the two phase-coherent pump pulses [black solid line in Fig. 2(c)]. In this simplified model, the population difference corresponds to the photoinduced band occupation variation, which is responsible for triggering the slow insulator-to-metal transformation. In the simulation, the electronic levels are excited by two phase-locked and temporally delayed pulses with Gaussian profiles with input parameters corresponding to the experimental ones. The phenomenological coherence time T_2 , which represents a dissipative timescale for the off-diagonal coherence (ρ_{01} and ρ_{10} terms), and the bare transition energy $\hbar\omega_{01}$ are left as free effective parameters optimized to match the observed redshift and spectral width variation. The best agreement is obtained for $T_2 = (5.6 \pm 1.0)$ fs and $\hbar\omega_{01} = (2.32 \pm 0.02)$ eV (see Sec. S6 in the SM for more details [29]). In Sec. S2C we also included in the model the possible change of optical properties induced by the first pump and experienced by the second one. Also in this case a nonzero decoherence time is required in order to account for the observed phenomenology.

The solutions of the OBE also suggest that, for nonzero T_2 , the observed redshift Δ linearly depends on the detuning $\delta\omega$ between the driving field frequency $\hbar\omega_p$ and the transition energy $\hbar\omega_{01}$. Additional experiments, performed at $T = 100$ K and varying the central frequency of the pump pulses, confirm the linear relation between Δ and $\delta\omega$ [Fig. 2(c) inset]. By fitting a linear regression to the experimental values of Δ , we estimate the position of the transition at $\hbar\omega_{01} = (2.37 \pm 0.01)$ eV at $T = 100$ K, in good agreement with the value obtained from the OBE numerical results. Taken together, these data demonstrate that the photoinduced IMT after 100 ps is controlled by the initial band population imbalance, which is in turn determined by the coherent dynamics of the many-body state $|\Psi\rangle$. The observed T_2 is nonzero and allows for the

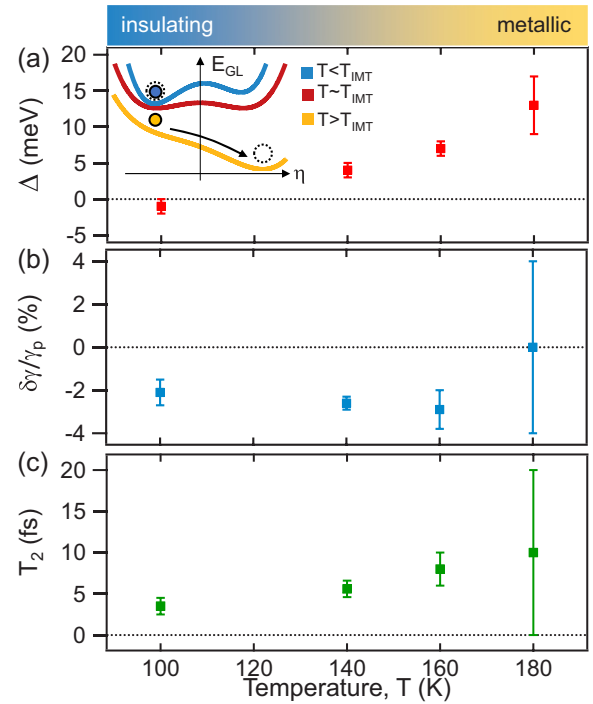


FIG. 3. Temperature dependence of electronic coherence parameters. (a) Measured energy shift and (b) relative spectral width variation as a function of temperature. (a) Inset: Free-energy diagram at different temperature values near the critical temperature T_{IMT} . (c) Coherence time values as a function of the temperature retrieved by applying the OBE analysis to the experimental results shown in (a) and (b). Where not reported, the error bar is smaller than the marker size.

exploitation of ultrashort pulses for coherent manipulation of the IMT.

A natural question arising from the reported evidence of coherent control of the IMT in V_2O_3 is whether T_2 can be increased in order to make coherent manipulation schemes more effective. An intriguing possibility is to exploit the coherent dynamics across the thermally driven transition at T_{IMT} . The flattening of the free-energy curve [see Eq. (1)] in the vicinity of the spinodal points, where one minimum becomes an inflection point of E_{GL} for $T > T_{\text{IMT}}$ [see the inset in Fig. 3(a)], can give rise to a slowing down of the η fluctuations, similarly to second-order phase transitions. Thus, the instantaneous free-energy configuration corresponding to the pump-induced $n_{a_{1g}}$ increase can contribute to enhancing the coherence time that regulates the time evolution of $|\Psi\rangle$. In Figs. 3(a) and 3(b), we report the Δ and $\delta\gamma/\gamma_p$ values measured for temperatures spanning the 100–180 K range. We note an increasing frequency shift Δ as T_{IMT} is approached. However, this effect may simply result from the continuous shift of the transition frequency $\hbar\omega_{01}$, which is also suggested by equilibrium optical properties [19]. In order to retrieve the values of T_2 , we performed the same analysis, based on OBE, as previously described. The results reported in Fig. 3(c) show a moderate increase of the coherence time up to a maximum value $T_2 = (8 \pm 2)$ fs. We note that the vanishing of the $\delta R/R(t_1)$ signal at $T \simeq T_{\text{IMT}}$ contributes to

the large uncertainty of the T_2 in the vicinity of the thermally driven IMT.

In conclusion, we have demonstrated the possibility of coherently controlling the orbital occupation of the a_{1g} and e_g^π levels in V_2O_3 . The extreme phase stability of the two phase-coherent pump pulses unveils signatures of coherent dynamics, such as detuning and time broadening of the $\delta R/R$ signal, even for electronic coherence times as short as 5 fs. The electronic coherence shows a tendency to increase in the vicinity of the thermal IMT. The orbital population change induced by the coherent excitation protocol drives the insulator-to-metal transition that takes place on the ~ 50 ps timescale. These findings suggest that the control of fluctuations of the electronic and structural degrees of freedom is key to enhancing electronic coherence and unlocks the gate for future advances in the coherent manipulation of solid-solid transitions. Experimentally, ultrafast coherent experiments probing the different degrees of freedom (e.g., phonons, spin excitations, orbital fluctuations) are needed to identify the main channels that control the electronic decoherence. This knowledge would indicate the most promising strategies, e.g., different excitation protocols or a combination with different external control parameters (chemical composition, strain, pressure, electric/magnetic fields), to preserve the electronic coherence on longer timescales. From a theoretical viewpoint,

microscopic models beyond master equations are expected to shed light on the way the many-body systems evolve from a coherent polarization state to a metastable macroscopic phase that can be thermodynamically described by a proper free-energy functional.

C.G., P.F., A.R., A.M., and S.M. acknowledge financial support from MIUR through the PRIN 2015 (Prot. 2015C5SEJJ001) and PRIN 2017 (Prot. 20172H2SC4_005) programs. C.G., S.P., and G.F. acknowledge support from Università Cattolica del Sacro Cuore through D.1, D.2.2, and D.3.1 grants. S.M. acknowledges partial financial support through the grant “Finanziamenti ponte per bandi esterni” from Università Cattolica del Sacro Cuore. M.M. acknowledges support from “Severo Ochoa” Programme for Centres of Excellence in R&D (MINCINN, Grant No. SEV-2016-0686). M.F. has received funding from the European Research Council (ERC) under the European Union’s Horizon 2020 research and innovation programme, Grant Agreement No. 692670 “FIRSTORM.” V.P., S.D.C., and G.C. acknowledge support by the European Union’s Horizon 2020 Programme under Grant Agreement No. 881603 Graphene Core 3. S.D.C. acknowledges financial support from MIUR through the PRIN 2017 Programme (Prot. 20172H2SC4)

-
- [1] D. M. Basov, R. D. Averitt, and D. Hsieh, Towards properties on demand in quantum materials, *Nat. Mater.* **16**, 1077 (2017).
- [2] S. Koshihara, T. Ishikawa, Y. Okimoto, K. Onda, R. Fukaya, M. Hada, Y. Hayashi, S. Ishihara, and T. Luty, Challenges for developing photo-induced phase transition (PIPT) systems: From classical (incoherent) to quantum (coherent) control of PIPT dynamics, *Phys. Rep.* **942**, 1 (2022).
- [3] M. Shapiro and P. Brumer, Coherent control of atomic, molecular, and electronic processes, *Adv. At. Mol. Opt. Phys.* **42**, 287 (2000).
- [4] A. H. Zewail, Femtochemistry: Atomic-scale dynamics of the chemical bond, *J. Phys. Chem. A* **104**, 5660 (2000).
- [5] T. S. Rose, M. J. Rosker, and A. H. Zewail, Femtosecond real-time observation of wave packet oscillations (resonance) in dissociation reactions, *J. Chem. Phys.* **88**, 6672 (1988).
- [6] R. M. Bowman, M. Dantus, and A. H. Zewail, Femtochemistry of the reaction: $IHgI^* \rightarrow [IHg \dots I]^{**} \rightarrow HgI + I$, *Chem. Phys. Lett.* **156**, 131 (1989).
- [7] E. D. Potter, J. L. Herek, L. Pedersen, Q. Liu, and A. H. Zewail, Femtosecond laser control of a chemical reaction, *Nature (London)* **355**, 66 (1992).
- [8] A. Assion, T. Baumert, M. Bergt, T. Brixner, B. Kiefer, V. Seyfried, M. Strehle, and G. Gerber, Control of chemical reactions by feedback-optimized phase-shaped femtosecond laser pulses, *Science* **282**, 919 (1998).
- [9] J. L. Herek, W. Wohlleben, R. J. Cogdell, D. Zeidler, and M. Motzkus, Quantum control of energy flow in light harvesting, *Nature (London)* **417**, 533 (2002).
- [10] Y. Matsubara, S. Ogihara, J. Itatani, N. Maeshima, K. Yonemitsu, T. Ishikawa, Y. Okimoto, S.-Y. Koshihara, T. Hiramatsu, Y. Nakano, H. Yamochi, G. Saito, and K. Onda, Coherent dynamics of photoinduced phase formation in a strongly correlated organic crystal, *Phys. Rev. B* **89**, 161102(R) (2014).
- [11] J. G. Horstmann, H. Böckmann, B. Wit, F. Kurtz, G. Storeck, and C. Ropers, Coherent control of a surface structural phase transition, *Nature (London)* **583**, 232 (2020).
- [12] H. Petek and S. Ogawa, Femtosecond time-resolved two-photon photoemission studies of electron dynamics in metals, *Prog. Surf. Sci.* **56**, 239 (1997).
- [13] S. Ogawa, H. Nagano, H. Petek, and A. P. Heberle, Optical Dephasing in Cu(111) Measured by Interferometric Two-Photon Time-Resolved Photoemission, *Phys. Rev. Lett.* **78**, 1339 (1997).
- [14] H. Petek, A. P. Heberle, W. Nessler, H. Nagano, S. Kubota, S. Matsunami, N. Moriya, and S. Ogawa, Optical Phase Control of Coherent Electron Dynamics in Metals, *Phys. Rev. Lett.* **79**, 4649 (1997).
- [15] W. Nessler, S. Ogawa, H. Nagano, H. Petek, J. Shimoyama, Y. Nakayama, and K. Kishio, Femtosecond Time-Resolved Study of the Energy and Temperature Dependence of Hot-Electron Lifetimes in $Bi_2Sr_2CaCu_2O_{8+\delta}$, *Phys. Rev. Lett.* **81**, 4480 (1998).
- [16] R. Atanasov, A. Haché, J. L. P. Hughes, H. M. van Driel, and J. E. Sipe, Coherent Control of Photocurrent Generation in Bulk Semiconductors, *Phys. Rev. Lett.* **76**, 1703 (1996).
- [17] A. Haché, Y. Kostoulas, R. Atanasov, J. L. P. Hughes, J. E. Sipe, and H. M. van Driel, Observation of Coherently Controlled Photocurrent in Unbiased, Bulk GaAs, *Phys. Rev. Lett.* **78**, 306 (1997).
- [18] P. Rozier, A. Ratuszna, and J. Galy, Comparative structural and electrical studies of V_2O_3 and $V_{2-x}Ni_xO_3$ ($0 < x < 0.75$) solid solution, *Z. Anorg. Allg. Chem.* **628**, 1236 (2002).

- [19] M. M. Qazilbash, A. A. Schafgans, K. S. Burch, S. J. Yun, B. G. Chae, B. J. Kim, H. T. Kim, and D. N. Basov, Electrodynamics of the vanadium oxides VO_2 and V_2O_3 , *Phys. Rev. B* **77**, 115121 (2008).
- [20] A. I. Poteryaev, J. M. Tomczak, S. Biermann, A. Georges, A. I. Lichtenstein, A. N. Rubtsov, T. Saha-Dasgupta, and O. K. Andersen, Enhanced crystal-field splitting and orbital-selective coherence induced by strong correlations in V_2O_3 , *Phys. Rev. B* **76**, 085127 (2007).
- [21] J.-H. Park, L. H. Tjeng, A. Tanaka, J. W. Allen, C. T. Chen, P. Metcalf, J. M. Honig, F. M. F. de Groot, and G. A. Sawatzky, Spin and orbital occupation and phase transitions in V_2O_3 , *Phys. Rev. B* **61**, 11506 (2000).
- [22] A. Ronchi, P. Franceschini, A. De Poli, P. Homm, A. Fitzpatrick, F. Maccherozzi, G. Ferrini, F. Banfi, S. S. Dhesi, M. Menghini, M. Fabrizio, J.-P. Locquet, and C. Giannetti, Nanoscale self-organization and metastable non-thermal metallicity in Mott insulators, *Nat. Commun.* **13**, 3730 (2022).
- [23] J. B. Goodenough, Anomalous properties of the vanadium oxides, *Annu. Rev. Mater. Sci.* **1**, 101 (1971).
- [24] J. B. Goodenough, Metallic oxides, *Prog. Solid State Chem.* **5**, 145 (1971).
- [25] M. K. Liu, B. Pardo, J. Zhang, M. M. Qazilbash, S. J. Yun, Z. Fei, J.-H. Shin, H.-T. Kim, D. N. Basov, and R. D. Averitt, Photoinduced Phase Transitions by Time-Resolved Far-Infrared Spectroscopy in V_2O_3 , *Phys. Rev. Lett.* **107**, 066403 (2011).
- [26] M. Sandri and M. Fabrizio, Nonequilibrium gap collapse near a first-order Mott transition, *Phys. Rev. B* **91**, 115102 (2015).
- [27] G. Lantz, B. Mansart, D. Grieger, D. Boschetto, N. Nilforoushan, E. Papalazarou, N. Moisan, L. Perfetti, V. L. R. Jacques, D. Le Bolloc'h, C. Laulhé, S. Ravy, J.-P. Rueff, T. E. Glover, M. P. Hertlein, Z. Hussain, S. Song, M. Chollet, M. Fabrizio, and M. Marsi, Ultrafast evolution and transient phases of a prototype out-of-equilibrium Mott-Hubbard material, *Nat. Commun.* **8**, 13917 (2017).
- [28] A. Ronchi, P. Homm, M. Menghini, P. Franceschini, F. Maccherozzi, F. Banfi, G. Ferrini, F. Cilento, F. Parmigiani, S. S. Dhesi, M. Fabrizio, J.-P. Locquet, and C. Giannetti, Early-stage dynamics of metallic droplets embedded in the nanotextured Mott insulating phase of V_2O_3 , *Phys. Rev. B* **100**, 075111 (2019).
- [29] See Supplemental Material at <http://link.aps.org/supplemental/10.1103/PhysRevB.107.L161110> for additional details regarding the spectral properties of the material and the optical excitation; the derivation and the numerical solution of the model based on optical Bloch equations; the choice of the experimental parameters to optimize coherent effects; the experimental setup; the analysis of the measurements performed at different temperatures; and the retrieval of the temperature-dependent coherence time.
- [30] D. Brida, C. Manzoni, and G. Cerullo, Phase-locked pulses for two-dimensional spectroscopy by a birefringent delay line, *Opt. Lett.* **37**, 3027 (2012).
- [31] J. Réhault, M. Maiuri, A. Oriana, and G. Cerullo, Two-dimensional electronic spectroscopy with birefringent wedges, *Rev. Sci. Instrum.* **85**, 123107 (2014).
- [32] A. Oriana, J. Réhault, F. Preda, D. Polli, and G. Cerullo, Scanning Fourier transform spectrometer in the visible range based on birefringent wedges, *J. Opt. Soc. Am. A* **33**, 1415 (2016).
- [33] F. Preda, A. Oriana, J. Réhault, L. Lombardi, A. C. Ferrari, G. Cerullo, and D. Polli, Linear and nonlinear spectroscopy by a common-path birefringent interferometer, *IEEE J. Sel. Top. Quantum Electron.* **23**, 88 (2017).
- [34] L. Dillemans, T. Smets, R. R. Lieten, M. Menghini, C.-Y. Su, and J.-P. Locquet, Evidence of the metal-insulator transition in ultrathin unstrained V_2O_3 thin films, *Appl. Phys. Lett.* **104**, 071902 (2014).
- [35] E. Abreu, S. Wang, J. G. Ramírez, M. Liu, J. Zhang, K. Geng, I. K. Schuller, and R. D. Averitt, Dynamic conductivity scaling in photoexcited V_2O_3 thin films, *Phys. Rev. B* **92**, 085130 (2015).